J. Phys. B: At. Mol. Opt. Phys. **32** (1999) 895–913. Printed in the UK PII: S0953-4075(99)94872-1

Electron angular distributions in low-energy (e, 2e) reactions

Jamal Berakdar†, John S Briggs‡, Igor Bray§ and Dmitry V Fursa§

† Max-Planck Institut für Mikrostrukturphysik Weinberg 2, 06120 Halle, Germany
‡ Theoretical Quantum Dynamics, Albert-Ludwigs-Universität, Hermann-Herder-Straße 3, 79104 Freiburg, Germany
§ Flinders University, GPO Box 2100, Adelaide 5001, Australia

Received 8 June 1998

Abstract. The fully differential cross section for the electron-impact ionization of atomic hydrogen is analysed at an incident energy of 27.2 eV. The cross sections are calculated using a variety of theoretical models whose predictions are compared. It is seen that, as at higher impact energies, the angular distribution basically consists of two peaks which, at first sight, can be assigned to binary and recoil processes. However we show that the similarity is somewhat illusory in that the shape and position of the two peaks depend sensitively on the detection geometry and the energy sharing between the two electrons. Furthermore, the final-state electron–electron repulsion and the effects of exchange symmetry contribute significantly to the form of the observed angular distributions.

1. Introduction

The coincident detection of two electrons following electron-impact single ionization of the hydrogen atom (e, 2e experiment) continues to provide the most detailed information on the fundamental quantum dynamics of the ionization process. The data also provide the most stringent test of theory, although unfortunately spin-resolved detection, which could test the separate singlet and triplet cross sections predicted by theory, is not yet feasible for this target. The parameters to be varied in the experiment are the incident energy E_i with respect to the ionization energy I and the way in which the excess energy ($E = E_i - I$) is shared between the two electrons. The former is most conveniently expressed in terms of the ratio (E_i/I) and the latter by the ratio E_a/E_b of the final-state energies of electrons a and b. By convention the faster of the two electrons is designated as electron a. The fundamental quantity of interest is the shape of the angular distribution of the electron emission as the above parameters are varied.

Experimental data have been presented for a variety of orientations of the vectors $\boldsymbol{k}_i, \boldsymbol{k}_a, \boldsymbol{k}_b$ (initial and final electron momentum vectors, respectively) designed to explore different aspects of the collision process. Perhaps the most extensive sequence of measurements has been performed in the geometry to be considered here, namely, that all three vectors $\hat{\boldsymbol{k}}_i, \hat{\boldsymbol{k}}_a, \hat{\boldsymbol{k}}_b$ lie in a plane. For fixed $\hat{\boldsymbol{k}}_a$ the orientation of $\hat{\boldsymbol{k}}_b$ in the plane is varied, keeping the energies $E_a = \frac{1}{2}k_a^2$, $E_b = \frac{1}{2}k_b^2$ fixed. It is perhaps remarkable, although by now well established, that for ionization of the hydrogen atom over the *complete range* of values of the ratios (E_i/I), E_a/E_b the angular distribution of electron b, for fixed electron a, almost always shows a simple double-peak structure. That this is so at high energy $E_i/I \gg 1$ and unequal energy-sharing $E_a/E_b \gg 1$ has been evident for a long time. Fragmentary evidence for the basic simplicity of

0953-4075/99/040895+19$19.50

the electron-impact ionization process also near threshold, i.e. where $E_i/I \sim 1$, and for equal energy-sharing $E_a/E_b \sim 1$ has been accumulating more recently.

At high energy and where $E_a/E_b \gg 1$, a glancing collision is made, imparting a small fraction of the incident energy to the target electron. Emergence close to the forward (beam) direction is due to an essentially free electron–electron collision giving rise to what is termed 'the binary peak'. Since the maximum angle of emergence of an initially-free electron is 90° to the beam direction, any electrons emerging at angles larger than this must involve the participation of the nucleus and therefore involve nuclear recoil. The simplest example of this is the emergence of the second peak, 'the recoil peak' in a first Born approximation (FBA) description of the collision. This arises from double collisions (Briggs 1989) in which the target electron, after being struck by the projectile electron, rebounds off the nucleus to emerge in backward directions.

The persistence of the basic features of binary and recoil peaks as threshold $E_i/I \to 1$ and equal energy-sharing $E_a/E_b \to 1$ are approached has been noted already (Brauner *et al* 1991, Berakdar *et al* 1996, Berakdar 1997). Despite this, it will be shown here that the similarity is somewhat illusory since additional complicating features do appear; the collision process is strongly influenced by the three-body nature of the collision, rather than being purely explicable in terms of single- or double-binary collisions. Furthermore, the effects of electron–electron repulsion in the final state and the differing structure of singlet and triplet cross sections (Brauner *et al* 1991) play a major role. Nevertheless, the two-peak, smooth structure of the ionization differential cross sections *is* preserved. Certainly this is connected to the fact that no resonance structures are possible for $E_i/I > 1$ for pure Coulomb-interacting particles (Simon 1978) and the fact that according to classical mechanics only a single passage through the triple-collision manifold is made for each ionizing event, i.e. the hyper-radius as a function of time possesses, if at all, a minimum and no maximum (Wannier 1953, Rost 1998). In the following we attempt to shed further light on the near-threshold ionization process by analysing more extensive data and comparing with a variety of theoretical methods. Atomic units are used throughout.

2. Theoretical models

There is quite a number of theoretical approaches to deal with the electron-impact ionization problem (Madison *et al* 1977, Whelan *et al* 1993, see also McCarthy and Weigold 1995 and references therein). In this work we focus on two particular methods which represent the analytical and the rather numerical theories, namely the Coulomb wavefunctions methods, as presented in section 2.1, and the convergent close-coupling (CC) method.

2.1. FBA, 2C, 3C, DS3C

The probability for two electrons to be emitted with energies E_a and E_b into the solid angles Ω_a and Ω_b following electron impact on atomic hydrogen is related to the triply differential cross section (TDCS)

$$\mathrm{TDCS}(E_a, E_b, \Omega_a, \Omega_b) = (2\pi)^4 \frac{k_a k_b}{k_i} |\mathcal{T}_{\mathrm{fi}}|^2, \tag{1}$$

where $\boldsymbol{k}_i$ is the momentum of the incident electron and $\mathcal{T}_{\mathrm{fi}}$ is the transition amplitude that can be written in the form

$$\mathcal{T}_{\mathrm{fi}}(\boldsymbol{k}_a, \boldsymbol{k}_b) = \langle \Psi^-_{\boldsymbol{k}_a, \boldsymbol{k}_b} | V_i | \Phi_{\boldsymbol{k}_i} \rangle. \tag{2}$$

Here $|\Phi_{\boldsymbol{k}_i}\rangle$ is the state vector of the three-body system in the initial channel which is chosen to be a product of an incoming plane wave representing the incident projectile electron and an undistorted 1s-state of atomic hydrogen.

Corresponding to this initial state, the perturbation potential V_i is

$$V_i = V_{\mathrm{ee}} + V_{\mathrm{eN}} = \frac{1}{|\boldsymbol{r}_a - \boldsymbol{r}_b|} + \frac{-1}{r_a}. \tag{3}$$

The coordinates $\boldsymbol{r}_a$ and $\boldsymbol{r}_b$ label the positions of the electrons with respect to the nucleus.

Combining (2) and (3) we can write the transition amplitude equation (2) as the sum of a scattering amplitude T_{ee} of the incident electron from the bound electron, i.e. from the potential V_{ee}, and a scattering amplitude T_{eN} from the proton (potential V_{eN}), i.e.

$$\mathcal{T}_{\mathrm{fi}}(\boldsymbol{k}_a, \boldsymbol{k}_b) = T_{\mathrm{ee}} + T_{\mathrm{eN}} := \langle \Psi^-_{\boldsymbol{k}_a,\boldsymbol{k}_b} | V_{\mathrm{ee}} | \Phi_{\boldsymbol{k}_i} \rangle + \langle \Psi^-_{\boldsymbol{k}_a,\boldsymbol{k}_b} | V_{\mathrm{eN}} | \Phi_{\boldsymbol{k}_i} \rangle. \tag{4}$$

Formally, the state vector $\langle \Psi^-_{\boldsymbol{k}_a,\boldsymbol{k}_b}|$, as it appears in equation (2), should be an exact eigenstate of the total three-body Hamiltonian at a fixed total energy E and with appropriate boundary conditions. The approximate expressions (for $\langle \Psi^-_{\boldsymbol{k}_a,\boldsymbol{k}_b}|$) we use in this study have the form

$$\begin{aligned}\Psi^-_{\boldsymbol{k}_a,\boldsymbol{k}_b}(\boldsymbol{r}_a, \boldsymbol{r}_b) \approx (2\pi)^{-3} \exp(\mathrm{i}\boldsymbol{k}_a \cdot \boldsymbol{r}_a + \mathrm{i}\boldsymbol{k}_b \cdot \boldsymbol{r}_b) \\ N_a\, {}_1F_1[\mathrm{i}\alpha_a, 1, -\mathrm{i}k_a(r_a + \hat{\boldsymbol{k}}_a \cdot \boldsymbol{r}_a)] \\ N_b\, {}_1F_1[\mathrm{i}\alpha_b, 1, -\mathrm{i}k_b(r_b + \hat{\boldsymbol{k}}_b \cdot \boldsymbol{r}_b)] \\ N_{ab}\, {}_1F_1[\mathrm{i}\alpha_{ab}, 1, -\mathrm{i}k_{ab}(r_{ab} + \hat{\boldsymbol{k}}_{ab} \cdot \boldsymbol{r}_{ab})],\end{aligned} \tag{5}$$

where N_j, $j \in \{a, b, ab\}$ are normalization constants, ${}_1F_1[a, b, x]$ is the confluent hypergeometric function, and $\boldsymbol{r}_{ab} = \boldsymbol{r}_a - \boldsymbol{r}_b$ is the interelectronic relative coordinate with $\boldsymbol{k}_{ab}$ being the momentum conjugate to this coordinate. The Sommerfeld parameters (α_j, $j = a, b, ab$) are generally momentum dependent and their functional form depends on the approximation adopted. The FBA is obtained from (5) by setting $\alpha_b = -1/k_b$, $\alpha_a \equiv 0 \equiv \alpha_{ab}$. Regarding the two electrons to move independently in the Coulomb field of the nucleus, their wavefunction is then a product of two Coulomb waves (this approximation is called hereafter 2C) corresponding to choosing the Sommerfeld parameters: $\alpha_b = -1/k_b$, $\alpha_a = -1/k_a$, $\alpha_{ab} \equiv 0$. Assuming the three-body system to consist of three spatially-independent two-body systems leads to a representation of the final state as a product of three two-body Coulomb waves (3C) (Garibotti and Miraglia 1980, Brauner *et al* 1989). In this case the Sommerfeld parameters are $\alpha_b = -1/k_b$, $\alpha_a = -1/k_a$, $\alpha_{ab} = 1/(2k_{ab})$. If we allow, within the aforementioned three two-body subsystems, for dynamical mutual screening we arrive at the DS3C (dynamically screened 3C) approximation. The derivation of the Sommerfeld parameters is quite complicated. Here we cite the explicit functional form of the product charges $Z_j = \alpha_j k_j$, $j \in \{a, b, ab\}$ for the case of atomic hydrogen (for more detail cf Berakdar (1996a, b) and Berakdar *et al* (1996c))

$$Z_{ba}(\boldsymbol{k}_a, \boldsymbol{k}_b) = [1 - (f\ g)^2 a^{b_1}]a^{b_2} \tag{6}$$

$$Z_a(\boldsymbol{k}_a, \boldsymbol{k}_b) = -1 + (1 - Z_{ba}) \frac{k_a^{1+a}}{(k_a^a + k_b^a)|\boldsymbol{k}_a - \boldsymbol{k}_b|} \tag{7}$$

$$Z_b(\boldsymbol{k}_a, \boldsymbol{k}_b) = -1 + (1 - Z_{ba}) \frac{k_b^{1+a}}{(k_a^a + k_b^a)|\boldsymbol{k}_a - \boldsymbol{k}_b|} \tag{8}$$

where the functions occurring in equations (6), (7) are defined as

$$f := \frac{3 + \cos^2(4\alpha)}{4}, \qquad \tan\alpha = \frac{k_a}{k_b} \tag{9}$$

$$g := \frac{|\boldsymbol{k}_a - \boldsymbol{k}_b|}{k_a + k_b} \tag{10}$$

$$b_1 := \frac{2k_a k_b \cos(\theta_{ab}/2)}{k_a^2 + k_b^2} \tag{11}$$

$$b_2 := g^2(-0.5 + \mu) \tag{12}$$

$$a := \frac{E}{E + 0.5}. \tag{13}$$

Here E is measured in atomic units and $\mu = 1.127$ is the Wannier index. The interelectronic relative angle θ_{ab} is given by $\theta_{ab} := (\cos^{-1} \hat{\boldsymbol{k}}_a \cdot \hat{\boldsymbol{k}}_b)$.

From equations (6)–(8) it is clear that when two particles approach each other (in momentum space) they experience their full two-body Coulomb interactions, whereas the third one 'sees' a net charge equal to the sum of the charges of the two close particles. When the two electrons recede from the nucleus in opposite directions and equal velocities (with respect to the nucleus) the electron–electron interaction is subsumed completely in an effective electron–nuclear interaction. In addition, it can be shown that the behaviour of the total ionization cross sections evaluated using the final state function equation (5) with the product charges equations (6)–(8) is compatible with the Wannier threshold law. We note here that the papers of Berakdar *et al* (1996) and Berakdar (1997) contain a typographical error in the equation for b_2 (12). There b_2 was erroreously given as $b_2 = g(-0.5 + \mu)$.

2.2. Convergent close-coupling (CCC)

The details of the CCC approach to ionization have been given by Bray and Fursa (1996). Briefly, the total wavefunction is written as an explicitly antisymmetric expansion using N square-integrable (L^2) states ϕ_n^N ($n = 1, \ldots, N$) with energies ϵ_n^N, obtained by diagonalizing the target Hamiltonian in a Laguerre basis. The target states obtained in this way have both negative and positive energies. With increasing N the negative-energy states converge to the true discrete target eigenstates, whereas the positive-energy pseudostates yield an increasingly dense discretization of the target continuum. Specifying the N states and the total energy E of the electron–atom scattering system is sufficient to define uniquely the CC equations. In the CCC method these take the form of coupled Lippmann–Schwinger equations (Bray and Stelbovics 1992).

The CC final states have the form of an asymptotically plane wave for one electron and an L^2 state for the other $\langle \boldsymbol{k}_f \phi_f^N|$. In other words, the bound (ϕ_f^N) electron completely shields the other electron ($\boldsymbol{k}_f$) from the nuclear field, irrespective of the electron energies or positions. Such boundary conditions are ideal for elastic and inelastic non-ionizing scattering. They seem to be inappropriate in the case of ionization, where two electrons escape to infinity. Nevertheless, in the CCC theory we identify ionization processes with the excitation of the positive-energy target pseudostates. The CC boundary conditions specify that only one electron is ever detected at infinity. This implies that the CC theory treats the two electrons as distinguishable, even though antisymmetry has been formally incorporated. This is also the reason why in the CC formalism the energy integration is from zero to E, whereas any theory that treats the two electrons as being identical has the energy integration end-point $E/2$.

Upon solution of the CC equations the scattering amplitudes $\langle \boldsymbol{k}_f \phi_f^N | T^S(E) | \phi_i^N \boldsymbol{k}_i \rangle$ are obtained, where S is the total spin. Though the amplitudes are calculated for each $S = 0, 1$ we may readily separate the contributions from the direct f and exchange g contributions by writing $T^S = f + (-1)^S g$. Typically we take i to be the initial ground state. For final states f corresponding to true discrete eigenstates ($\phi_f^N = \phi_f, \epsilon_f^N = \epsilon_f < 0$) we use the calculated

amplitudes directly to obtain experimentally measured discrete excitation quantities. In the case of ionization we form the (e, 2e) amplitudes from

$$\mathcal{T}_{\rm fi}^{SN}(\boldsymbol{q},\boldsymbol{k}) = \langle \boldsymbol{q}_f^{(-)}|\phi_f^N\rangle\langle \boldsymbol{k}_f\phi_f^N|T^S(E)|\phi_i^N\boldsymbol{k}_i\rangle, \tag{14}$$

where $\boldsymbol{q}_f^{(-)}$ is a Coulomb wave of energy $q^2/2 = \epsilon_f^N$ (Bray and Fursa 1996), and use (1) to generate the differential cross sections. Writing the integrated cross section for excitation of the state ϕ_n^N as $\sigma_n^{SN} = |\langle \mathbf{k}_n\phi_n^N|T^S(E)|\phi_i^N\boldsymbol{k}_f\rangle|^2$ the total ionization cross section is given by

$$\sigma_{\rm I}^{NS} = \sum_{n:0<\epsilon_n^N<E} \sigma_n^{SN} \tag{15}$$

$$\equiv \int_0^E {\rm d}e \frac{{\rm d}\sigma}{{\rm d}e}^{SN}(e) \tag{16}$$

$$= \int_0^{E/2} {\rm d}e \left[\frac{{\rm d}\sigma}{{\rm d}e}^{SN}(e) + \frac{{\rm d}\sigma}{{\rm d}e}^{SN}(E-e)\right]. \tag{17}$$

Equation (15), and its equivalent form (16) that defines, using (14), the singly differential cross section (SDCS) (Bray and Fursa 1996), leads to excellent agreement with experiment for the total ionization cross section and its spin asymmetry (Bray and Stelbovics 1993). The simple rearrangement (17) shows that when calculating the total ionization cross section we have a sum of two different cross sections that belong to the same ionization process. The first ($\mathcal{T}_{\rm fi}^{SN}(\boldsymbol{q},\boldsymbol{k})$) is obtained from excitation of pseudostates with energy $e < E/2$, and the second ($\mathcal{T}_{\rm fi}^{SN}(\boldsymbol{k},\boldsymbol{q})$) from pseudostates with energy $E - e$. Generally, we find that the latter cross sections are much smaller than the former. In fact, Bray (1997) suggested that for infinite N the cross section for the excitation of pseudostates with energy greater than $E/2$ should be zero, leading to a step function in the SDCS. Whenever the size of the step is substantial, i.e. the $\frac{{\rm d}\sigma}{{\rm d}e}^{SN}(E/2) \gg 0$, the calculated $\frac{{\rm d}\sigma}{{\rm d}e}^{SN}(e)$ shows unphysical oscillation as a function of e. Since, after integration over all the angles of the TDCS the $\frac{{\rm d}\sigma}{{\rm d}e}^{SN}(e)$ is obtained, we immediately know that any particular TDCS is likely to be in substantial magnitude error. This problem may be avoided if the true SDCS happens to be known, and may be used to rescale the CCC TDCS by the ratio of the true and the calculated SDCS. The rescaling procedure says nothing about the accuracy of the shape or magnitude of any particular TDCS, its utility relies on the CCC TDCS having the correct shape for all possible angular distributions in the full space of the two electrons. If this is true then it guarantees correct magnitudes for all of the TDCS.

In the present case we provide CCC results from a 75-state calculation. For each target space $l \leqslant 5$ there are $15 - l$ states with the Laguerre λ_l fall-off factor ($\approx$1.2) chosen so that there was a state with energy 6.8 eV. Such a choice of states also leads to energy levels near 2 and 4 eV, see figure 1(*a*). Thus, we aim for greatest accuracy for the equal energy-sharing case, and rely on interpolation (Bray and Fursa 1996) to be sufficiently accurate at the other two energies.

Upon solution of the CC equations we obtain the integrated cross sections for the excitation of states with energy less than E. We use the cross section for the positive-energy states to define the SDCS, see figure 1(*b*). The raw (75) results are those according to (16) and are clearly unphysical indicating a lack of convergence. Yet the integral, from zero to E, yields 1.69 a_0^2, in agreement with the experimental value of Shah *et al* (1987). We need to have a way to estimate the raw result in the case of infinite N, which will have a step at $E/2$. We do so according to the given prescription (Bray 1997), where we assume that the true SDCS is well described by a quadratic. The integral and point of symmetry leave one more condition to define the quadratic uniquely. As in the case of electron-impact ionization of helium the e–H SDCS(e, E) at zero secondary energy e varies very slowly with E. This is because this cross

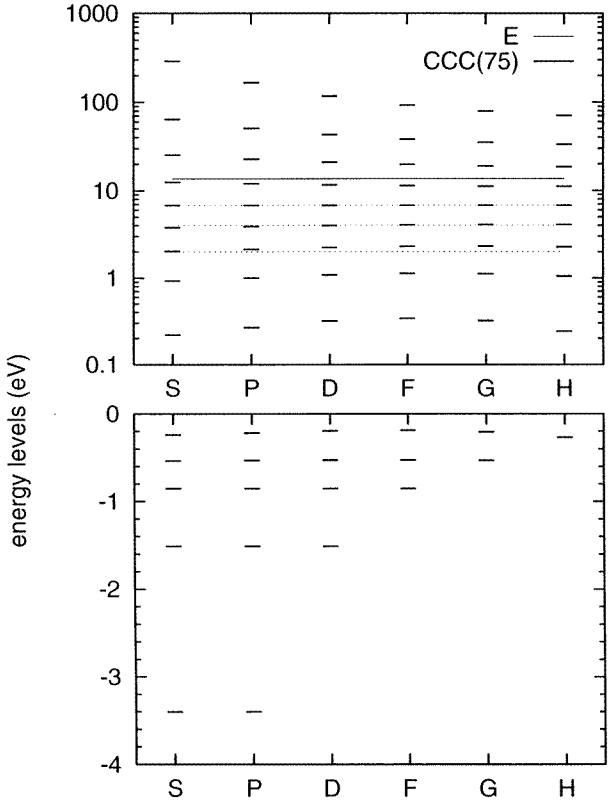

Figure 1. (*a*) Excited-state energy levels occurring in the 75-state CCC calculation. Only states with energies less than the total (excess) energy E are open. The dotted lines indicate 2, 4 and 6.8 eV. (*b*) The singly differential cross section (SDCS) as obtained from the 75-state CCC calculation. The raw(75) results correspond to equation (16). The CCC(75) correspond to equation (17). The CCC(∞) estimate is obtained by assuming the true SDCS is well described by a quadratic, see text. The factor differences between the CCC(∞) and CCC(75) curves at 2, 4 and 6.8 eV are 0.77, 0.88 and 1.99, respectively.

section is dominated by the interaction of the very slow ejected electron with the residual ion, and is largely independent of the fast electron leaving with energy E. To find the SDCS(0, E) for the present case of $E = 0.5$ au we look to the near-threshold region. From figure 2(*b*) of Bartschat and Bray (1996) which presents σ_1/E and the study of the e–H SDCS presented by Konovalov *et al* (1994) we take the value of SDCS(0, E) to be 0.4 a_0^2 eV^{-1}, which we believe to be accurate from threshold through to near 60 eV. This leads to the estimate of the SDCS represented by the CCC(∞) curve given in figure 1(*b*). The raw(∞) step function (not presented) is CCC(∞) from 0 to $E/2$ and zero from $E/2$ to E. The difference between the CCC(∞) and CCC(75) curves gives us the scaling factors of 0.77, 0.88 and 1.99 at 2, 4 and 6.8 eV, respectively.

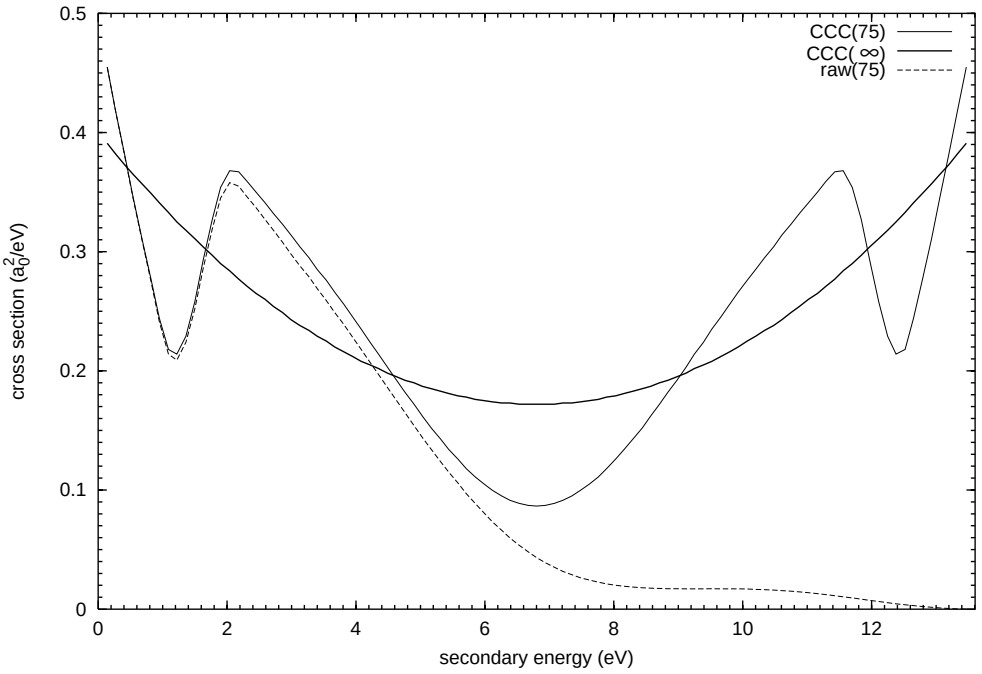

Figure 1. (Continued)

3. Interpretation of the spectra

In this section we analyse the angular distributions of the emitted electrons for a selected set of scattering geometries. We choose a coordinate system in which the x-axis is aligned along $\hat{\boldsymbol{k}}i$. The escaping electrons are detected in a coplanar geometry, i.e. $\boldsymbol{k}_i \cdot (\boldsymbol{k}_a \times \boldsymbol{k}_b) = 0$. The z-axis is along the direction perpendicular to the scattering plane, i.e. parallel to $\hat{\boldsymbol{k}}_a \times \hat{\boldsymbol{k}}_b$. The polar and azimuthal angles of the vector $\boldsymbol{k}_a$ ($\boldsymbol{k}_b$) are denoted by θ_a, ϕ_a (θ_b, ϕ_b), respectively. In what follows the polar angles are fixed to $\theta_a = \pi/2 = \theta_b$. This choice of coordinates enables us to show the full range of the angular distribution $\phi_b \in [0, 360^\circ]$ with the specification of only one angle (ϕ_a).

To get an insight into the kinematics of the ionization process we will inspect the recoil momentum of the proton left behind, $\boldsymbol{k}_{\rm ion}$, which is determined by the conservation law of linear momentum to be

$$\boldsymbol{k}_{\rm ion} = \boldsymbol{k}_i - \boldsymbol{k}_a - \boldsymbol{k}_b. \tag{18}$$

It is important to note here that for a given incident energy $E_i = k_i^2/2$ and a fixed energy $E_b = k_b^2/2$ of one of the electrons we determine the energy E_a, and hence the momentum $k_a = \sqrt{2E_a}$ from the energy conservation law $E_a = E_i - \epsilon - E_b$ where ϵ is the (positive) binding energy of H(1s), i.e. the momentum distribution of initial state is implicitly taken into account in equation (18). For $E_i \gg \epsilon$ the bound electron can be regarded as stationary from the view point of the projectile.

For atomic hydrogen there are, as yet, no reported spin-resolved TDCS measurements. Thus we are obliged to average statistically over the spin degrees of freedom. In the present reaction the TDCS is a statistical mixture of singlet (TDCS$^{\rm s}$) and triplet (TDCS$^{\rm t}$) cross sections,

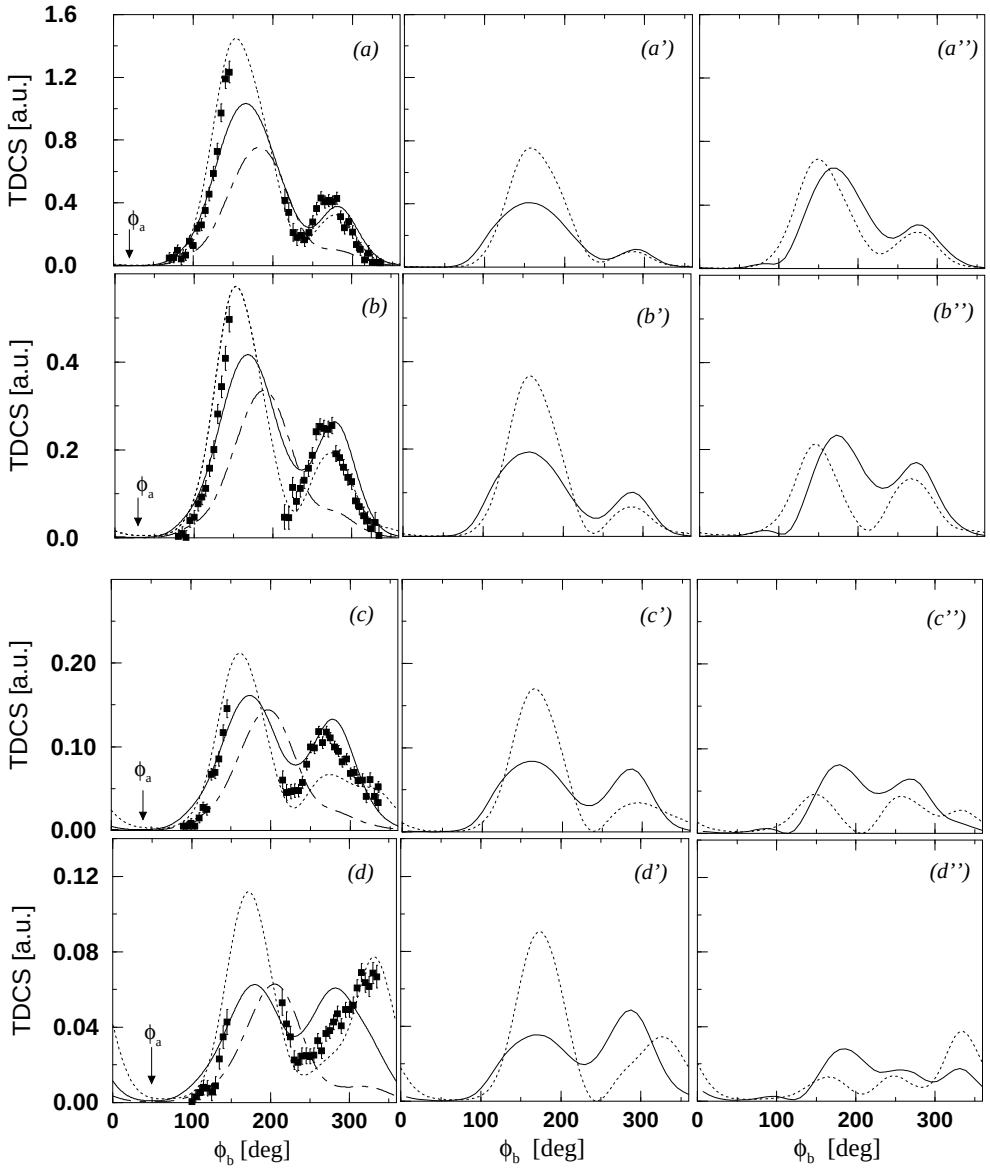

Figure 2. The spin-averaged angular distribution of an electron ejected with 2 eV following the electron-impact ionization of atomic hydrogen. The incident energy is chosen as $E_i = 27.2$ eV. The projectile electron is detected in coincidence with the ejected electron and in the plane spanned by $\boldsymbol{k}_b$ and $\boldsymbol{k}_i$. The scattering angle ϕ_a (indicated by an arrow) is fixed at (*a*) $\phi_a = 20^\circ$, (*b*) $\phi_a = 30^\circ$, (*c*) $\phi_a = 40^\circ$ and (*d*) $\phi_a = 50^\circ$. The DS3C (thick solid curve), 3C (dash-dotted curve), and CCC (dotted curve) are shown along with the experimental data (full squares) (Berakdar *et al* 1996). The CCC results have been multiplied by a factor of 0.76. The experimental data are inter-normalized, uncertainty in the relative height of the peaks is ≈7%. The singlet and triplet cross sections corresponding to the calculations in (*a*)–(*d*) are shown in (a')–(d') and (a'')–(d''), respectively (the results for the 3C calculations are not shown here).

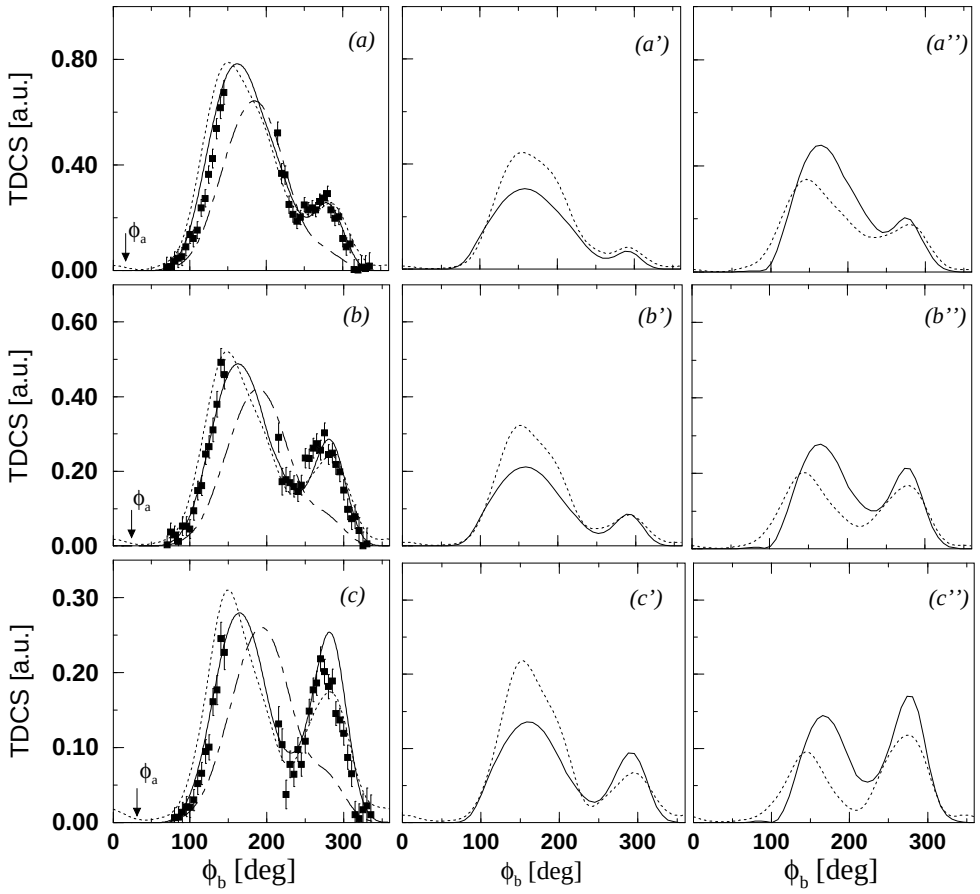

Figure 3. The same scattering geometry and the same notation as in figure 2, however, the ejected electron energy is chosen to have 4 eV. The angles of the scattered electrons in (*a*)–(*c*) are respectively chosen as $\phi_a = 16^\circ, 23^\circ, 30^\circ$. The inter-normalized experiments (full squares) are provided by Röder (1996). The CCC results have been multiplied by a factor of 0.88.

i.e.

$$\begin{aligned}\mathrm{TDCS}(E_a, E_b, \Omega_a, \Omega_b) &= \tfrac{1}{4}\mathrm{TDCS}^{\mathrm{s}} + \tfrac{3}{4}\mathrm{TDCS}^{\mathrm{t}} \\ &= \tfrac{1}{4}|f+g|^2 + \tfrac{3}{4}|f-g|^2 \end{aligned} \tag{19}$$

where f and g are the direct and exchange scattering amplitudes. In the case of the CCC theory there are two such cross sections, one from $\mathcal{T}_{\mathrm{fi}}^{SN}(\boldsymbol{q}, \boldsymbol{k})$ and the other from $\mathcal{T}_{\mathrm{fi}}^{SN}(\boldsymbol{k}, \boldsymbol{q})$, which are summed as in (17). Note that, from figure 1(*b*) it is clear that the latter contributes substantially only for the equal energy-sharing case.

In figures 2(*a*)–(*d*) the angular distributions of the slower electron, *b*, are scanned for different fixed angles, ϕ_a, of the other electron (indicated by arrows in the figures) where $\phi_a = 20^\circ, 30^\circ, 40^\circ, 50^\circ$, respectively. The energy of electron *b* is $E_b = 2$ eV, so that $E_a = 11.6$ eV. Generally, the measured spectra are very well reproduced by the CCC and DS3C results, except for figure 2(*d*) where clear discrepancies between the DS3C and the data are observed around $\phi_b \approx 300^\circ$. The 3C theory predicts almost equal shape for the

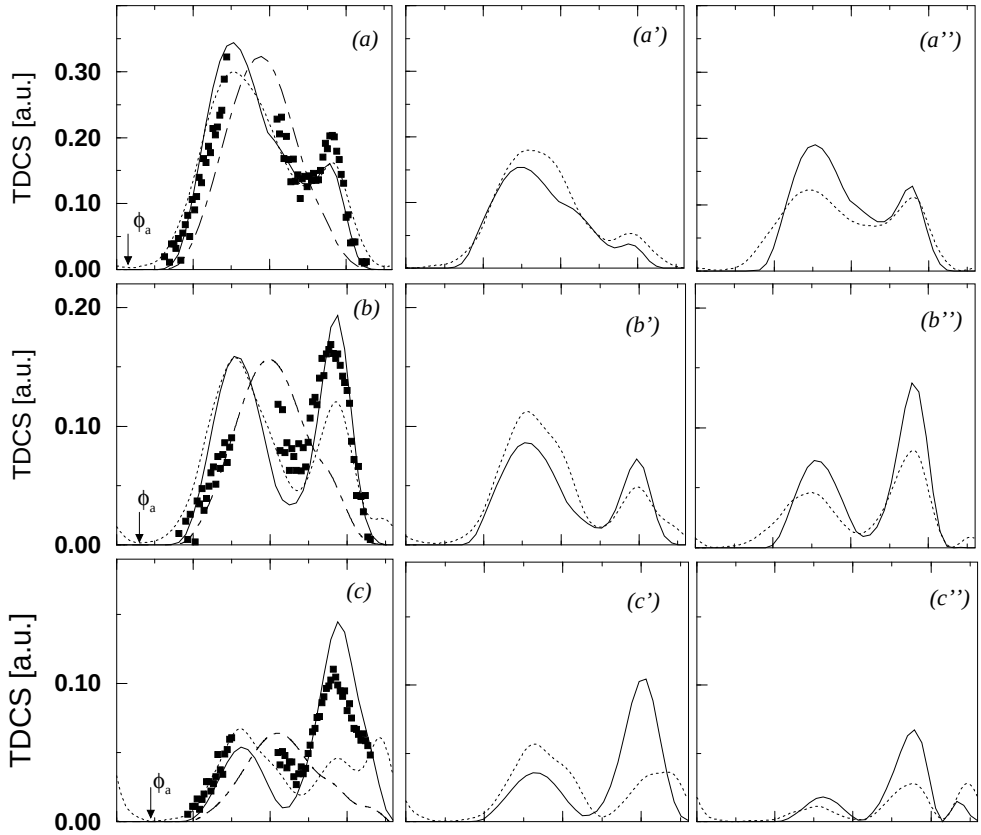

Figure 4. The same geometry and the same notation as in figure 2 for the equal energy-sharing case. The angle ϕ_a (indicated by an arrow) is fixed at (*a*) $\phi_a = 15^\circ$, (*b*) $\phi_a = 30^\circ$, (*c*) $\phi_a = 45^\circ$, (*d*) $\phi_a = 70^\circ$, and (*e*) $\phi_a = 90^\circ$. The experimental data (full squares) as taken from Brauner *et al* (1991). The CCC results have been multiplied by a factor of 1.99. The experiments are inter-normalized (Röder 1996).

cross section for all the cases depicted in figures 2(*a*)–(*d*) and is clearly at variance with the experimental findings. The failure of the 3C model in this geometry has been traced back to a wrong weighting of the amplitudes $T_{\rm eN}$ and $T_{\rm ee}$, i.e. a dominance of the former, which results in a spurious interference behaviour (Brauner *et al* 1991, Berakdar *et al* 1996). In other words, the observed spectra in figures 2(*a*)–(*d*) (and figures 3(*a*)–(*c*) as well) are the result of a subtle interference between the scattering from the nucleus and from the initially bound electron. Exchange effects were found to be of minor importance in this case of asymmetric energy-sharing (Berakdar 1997, Berakdar *et al* 1996). The double-peak structure of the cross section, as noted in the introduction, shows similarities with the binary-recoil-peak shape of the angular distributions at high energies (Ehrhardt *et al* 1986), i.e. the observed peaks tend to be localized around $\phi_b = \pm\hat{\boldsymbol{q}}$ where $\hat{\boldsymbol{q}}$ is the momentum transfer direction.

As shown already in Berakdar *et al* (1996) the designation recoil and binary appears justified by the near-coincidence of these peaks with respectively the maximum and minimum of the *recoil ion momentum* (these positions are distinctively different from $\pm\hat{\boldsymbol{q}}$). Although the magnitudes of both peaks diminish as ϕ_a increases, corresponding to an overall smaller

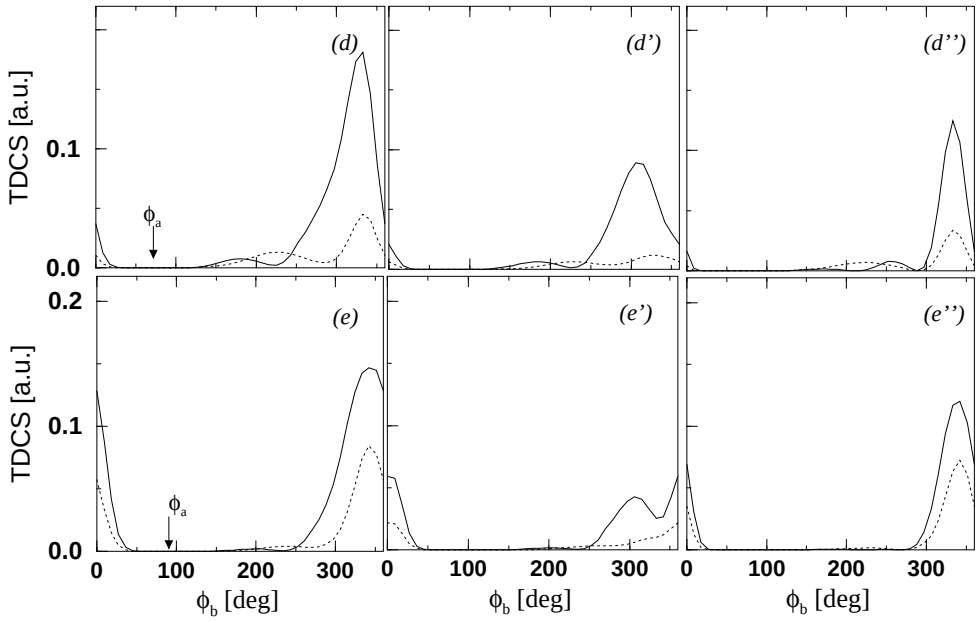

Figure 4. (Continued)

probability of large angle scattering, the relative heights of the two peaks appears to change also and there are subtle changes in the position and shape of the binary peak. The relative increase of the binary peak (in figure 2 the peak located near $\phi_b \approx 300^\circ$) as ϕ_a increases from 20° to 50° is in line with the general feature that single binary peaks emerge from the three-body background preferentially when the momentum transfer is largest, i.e. for large angle scattering of the primary electron. The apparent change in shape of the binary peak is hitherto unexplained. Its origin can be traced to the shape of the separate singlet and triplet contributions displayed in figures 2(a')–(d') and figures 2(a'')–(d''). For $\phi_a = 20^\circ$ and 30° the triplet and singlet have roughly the same smooth two-peak structure in both CCC and DS3C calculations, in fact exchange effects are of minor importance in this geometry. However, at $\phi_a = 40^\circ$ and 50° in CCC and $\phi_a = 50^\circ$ in DS3C, a new minimum appears in the triplet scattering, which splits the binary peak into two. This is the reason for the apparent shift of the binary peak closer to the forward direction in the experimental data of figure 2(d). Here it appears that the CCC represents better the dominance of triplet scattering near $\phi_b = 320^\circ$ (see figure 2(d)) which gives rise to this shift. The dip in the triplet cross section occurs for $E_a = 11.6$ eV, $E_b = 2$ eV and at an angle such that the two electrons are emitted symmetrically on opposite sides of the beam direction in the collision plane. As was shown in Brauner *et al* (1991) for *equal* energy electrons the triplet cross section vanishes identically at this point and gives rise to structure in the spin-averaged cross section. The dips in figures 2(c'') and (d'') represent the onset of this zero, although the cross section remains finite since the energies are not equal.

One further feature in figure 2 deserves mention. This is the near-vanishing of the cross sections when the two electrons emerge at roughly the same angle. It is directly due to the electron–electron repulsion which maximizes when the two electrons emerge in the same direction. This is the reason why the 'triplet dip' is not seen in figures 2(a) and (a'') and

figures 2(*b*) and (*b*′). There it occurs where the cross section is vanishingly small due to inter-electronic repulsion.

The CCC calculations presented in figures 2(*b*)–(*d*) reveal a small shoulder at $\phi_b \approx 330^\circ, 306^\circ, 290^\circ$, respectively. This behaviour persists for the equal energy-sharing case. As demonstrated below, the reason for this structure is not a numerical artifact, e.g. bad convergence, but it is most probably due to an overemphasized triplet scattering (see below).

In figures 3(*a*)–(*c*) the energy of the ejected electron is increased to $E_b = 4$ eV with E_a reduced to 7.6 eV. Again we notice the very good agreement between the spin-averaged CCC, DS3C and the experimental data. The main feature of figure 3 is the relative increase of the binary peak as ϕ_a increases, as in figure 2. Note that, since the energies of the two electrons are now more equal (7.6 eV and 4 eV), the 'hole' in the cross section around $\phi_a \approx \phi_b$ is larger than in figure 2. Since the data extend only to $\phi_a = 30^\circ$ the dip in the triplet cross section is barely evident in figures 3(*c*) and (*c*′) and not evident in the data, precisely due to the repulsive hole in the cross section. As in the case of figure 2, the triplet and singlet cross sections reveal a similar shape to the spin-averaged cross sections. In fact it turned out that (within the DS3C theory) in the case of figures 2 and 3 the direct scattering amplitude f dominates over g.

The experimental data depicted in figures 2(*a*)–(*d*) and figures 3(*a*)–(*c*) are inter-normalized, i.e. the magnitude of the cross section at a certain ϕ_a relative to another ϕ_a is determined. The CCC, DS3C and the 3C treatments agree remarkably well on the absolute

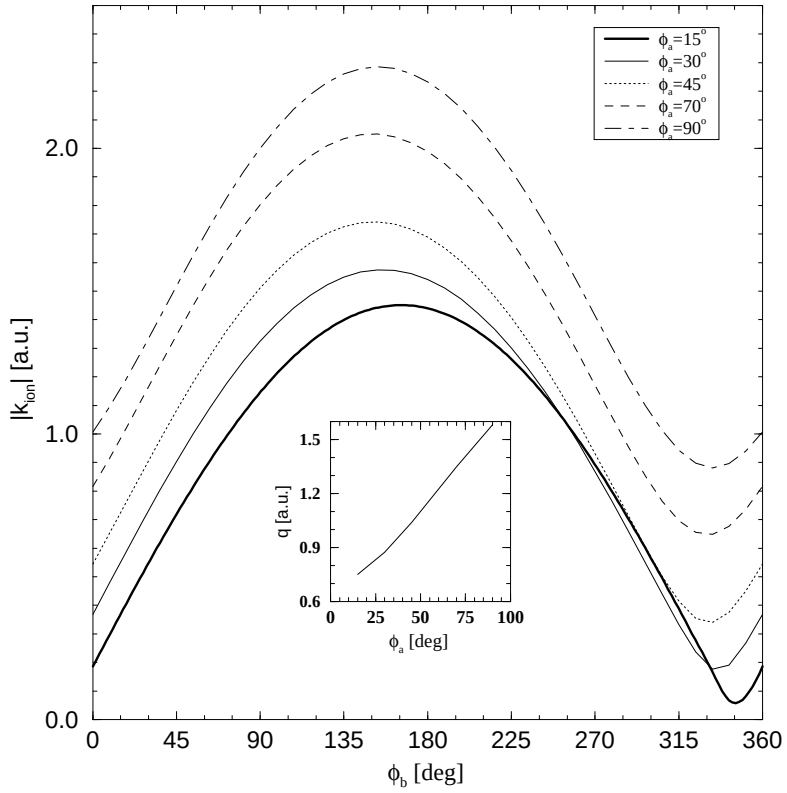

Figure 5. The recoil-ion momentum $k_{\rm rec}$ as a function of the emission angle ϕ_b for the cases of figure 4. The inset shows the variation of the momentum transfer q with the angle ϕ_a.

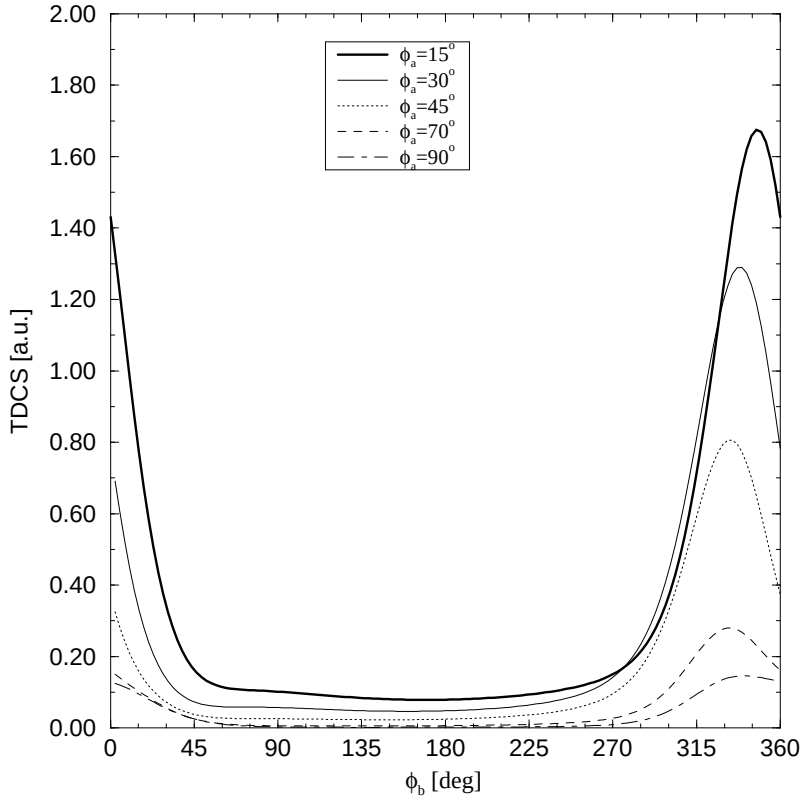

Figure 6. The spin-averaged cross section for the collision geometry of figure 4 as predicted by the FBA.

value of the cross sections, provided the CCC results are scaled as explained in the previous section.

In figures 4(*a*)–(*e*) the angular distributions for equal-energy electrons $E_a = E_b = 6.8$ eV are shown. Again there is overall agreement between experiment and the spin-averaged CCC and DS3C theories. The CCC results have been scaled by multiplication with factor 1.99, as stated earlier. The theory again correctly reproduces the increase of the binary peak maximum as ϕ_a increases, exactly as for unequal energy-sharing. Since electron repulsion maximizes for equal energies, the 'hole' for $\phi_a \approx \phi_b$ now has an angular width of nearly 90° and in the DS3C case is identically zero when $\phi_a = \phi_b$. This has the consequence that the 'triplet dip' which is a true zero in this equal-energy case, is not evident until $\phi_a = 30°$ (CCC) and $\phi_a = 45°$ (DS3C) (figures 4(b'') and (c'')). The zero is seen clearly in figure 4(c'') around $\phi_b = 315°$ and splits the binary peak into two. The CCC predicts a minimum in the spin-averaged cross section due to this effect, however, the different relative magnitudes of singlet and triplet in the DS3C case leads to a slight hint of a shoulder near 315° in the binary peak. An optimistic observer can see the same hint of a shoulder in the experimental data of figure 4(*c*). In figures 4(*d*) and (d'') ($\phi_a = 70°$), the triplet zero occurs at $\phi_b = 290°$ and again leads to a dip in the spin-averaged cross section for CCC, but merely a shoulder in the DS3C case. As ϕ_a increases to $\phi_a = 90°$ the triplet zero is 'overkilled' by the inter-electronic repulsion.

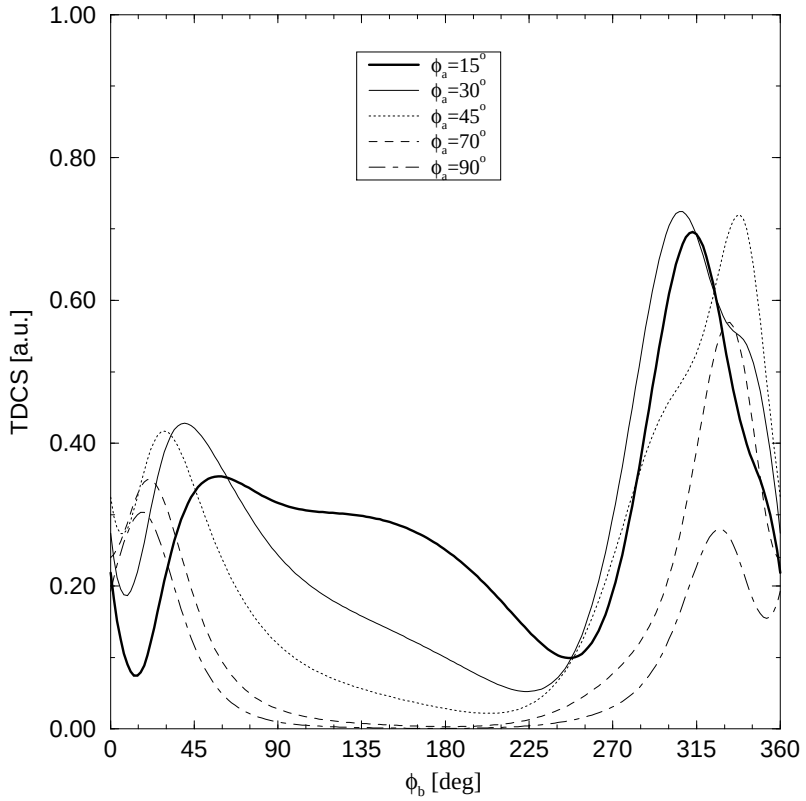

Figure 7. The same geometry as in figure 6, however, the calculations for the spin-averaged cross section have been performed with the 2C model.

In order to try to understand the behaviour of angular distributions in more detail, it is often useful to compare simpler theories, where certain interactions are ignored, with the predictions of the more complicated DS3C and CCC theories. This we will do with specific reference to figure 4 and equal energy electrons. First, it is important to show the magnitude of $k_{\rm ion}$ as a function of ϕ_b as is done in figure 5. Generally, with increasing ϕ_a the momentum absorbed by the proton increases. Accordingly, the momentum transfer q increases when ϕ_a becomes larger (see inset in figure 5). It is probably remarkable that this trend is reflected by the TDCS becoming smaller with increasing q, since this behaviour is anticipated for soft collisions and high impact velocity.

The minimum recoil momentum is shifted with respect to $\hat{\boldsymbol{q}}$ (assuming a stationary free target electron), for example for $\phi_a = 45^\circ$ this minimum occurs near $\phi_b = 330^\circ$ (for a stationary free target electron it would be at 315°) which justifies the association of the experimental peak near this position with single-binary scattering. The maximum recoil occurs when $\phi_b \approx 150^\circ$, again seemingly justifying the association of the peak in the experimental data near this position as arising from an interaction with the nucleus.

In high-energy (e, 2e) the 'recoil' peak does occur at the maximum in $k_{\rm ion}$ (Ehrhardt *et al* 1985). Since this peak is also present in the FBA, where only the slow electron interacts with the nucleus, it has been interpreted (Briggs 1989) as arising from the initially-bound electron

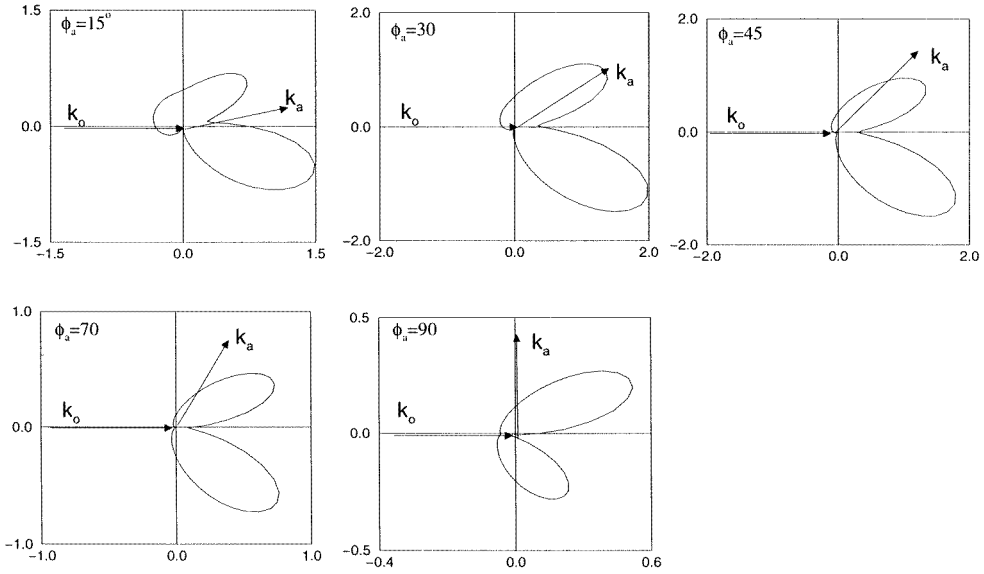

Figure 8. The singlet cross sections for the case of figure 7.

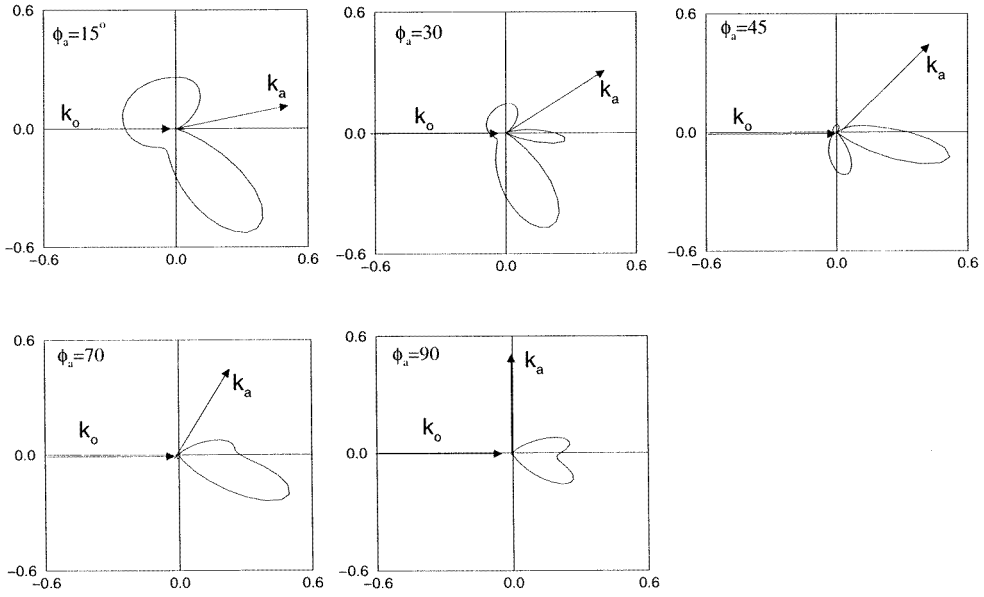

Figure 9. The triplet cross sections for the case of figure 7.

recoiling off the nucleus after having experienced a direct encounter with the projectile. At the low energy considered here we shall see that the 'recoil' peak has a more subtle origin.

The FBA results are shown in figure 6. They consist essentially of the binary peak, with a very flat cross section in the region of maximum nuclear recoil. The heights of the binary

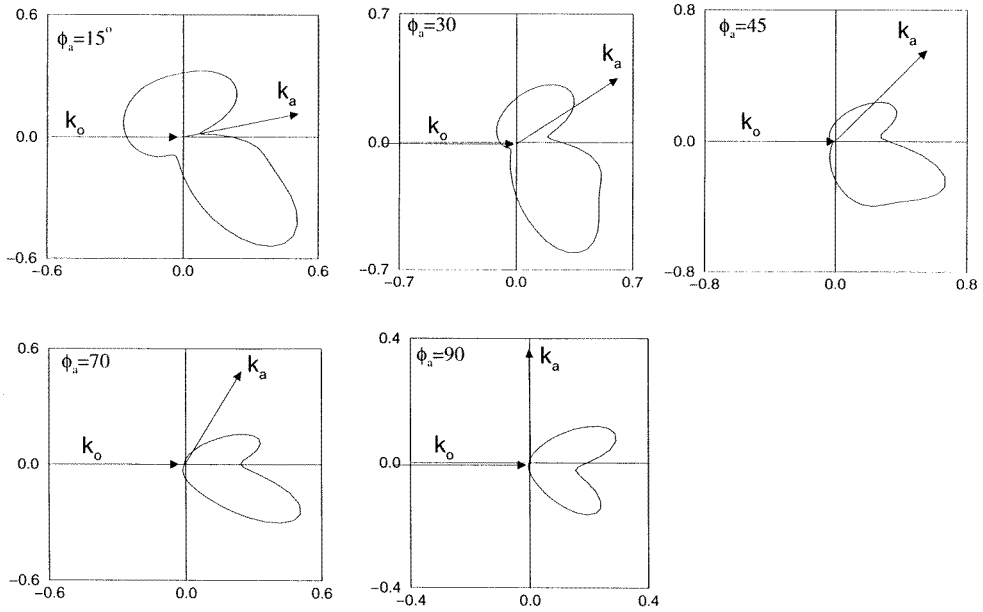

Figure 10. The statistical average of singlet and triplet as displayed in figures 8 and 9.

peaks decrease monotonically as q increases (cf inset in figure 5). In the FBA the electrons, although of identical energy, are treated unequally. The necessary symmetry is restored by the 2C approximation although the electron–electron repulsion in the final state, which carves out the hole in the cross section, is still ignored.

It should be noted that in both the FBA and the 2C approaches the amplitude T_{eN} for scattering from the nucleus vanishes identically due to orthogonality of different target states. Nonetheless this same scattering is mediated by the projectile–nucleus Coulomb wave in the 2C approximation.

Within the 2C model, the heights of the binary peaks (figure 7) as q increases (cf inset figure 5) do not follow an obvious trend as in the FBA (figure 6). In addition, the angular distribution predicted by the 2C cross section (figure 7) shows a new peak near $\phi_b < 45^\circ$, i.e. the two electrons emerge preferentially in nearly the same direction but well away from the position of maximum nuclear recoil.

The reason for this can be seen from figures 8–10, where we plot the 2C results in polar form for the complete range of angles $\phi_a = 15^\circ$, 30°, 45°, 70° and 90°. The separate contributions of singlet and triplet scattering are shown in figures 8 and 9. Considering first the singlet cross section, one sees that for $\phi_a = 15^\circ$ there is the binary peak and a back-scattering lobe reminiscent of the recoil peak in high-energy scattering (it appears near the maximum in k_{ion}). In addition however there is a further lobe, roughly symmetric to the binary lobe in the forward direction. As ϕ_a increases the 'recoil' contribution disappears and the near-symmetric two-lobe structure only remains. This indicates occupation preferentially of some spatial symmetry, as yet unidentified. The triplet cross section appears rather different (figure 9). However on closer inspection, one recognizes that the pattern is the same as for the singlet case, except that the requirements of antisymmetry lead to identical zeros at $\phi_b = \phi_a$ and $\phi_a = (360^\circ - \phi_a)$. The statistical average of the two cross sections is shown in figure 10 and, as one can see, for

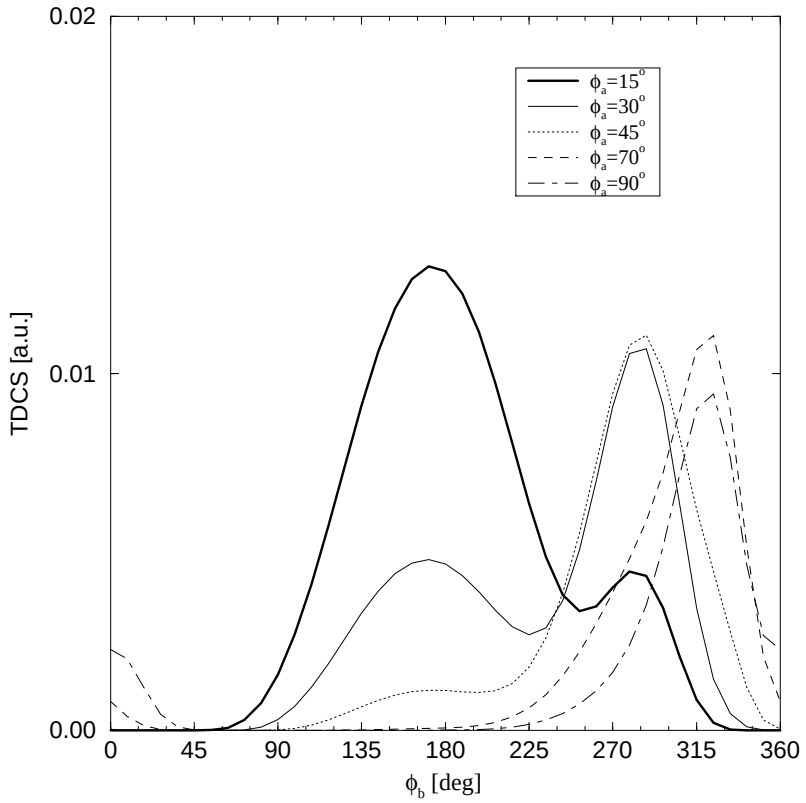

Figure 11. The same geometry as in figure 7 (and figure 4). The spin-averaged TDCS have been evaluated by multiplying the 2C results with the $|N_{ab}|^2$ factor (cf equation (5)).

example by comparing the linear plot of figure 7 with figure 4, the positions of the two peaks in the 2C result are not in agreement with experiment.

However, one key ingredient is missing from the 2C calculations, namely the electron–electron repulsion of the two free electrons in the final channel. This effect is most easily taken into account by multiplying the cross sections by $|N_{ab}|^2$, where N_{ab} is the normalization factor of the electron–electron two-body Coulomb wave (cf equation (5)). This *ad hoc* procedure has been used by several authors (Botero and Macek 1994, Röder *et al* 1996). This Coulomb density of states (CDS) factor peaks when the electrons are oppositely directed, $\phi_b = (180^\circ + \phi_a)$, and is zero for $\phi_b = \phi_a$. As shown in figure 11, when the 2C results are multiplied by this factor it carves out the repulsive hole in the cross section, shifting the position of the two peaks significantly. Remarkably, as seen from figure 11, the two peaks now appear in the same positions as observed in the experiment. In particular, one peak is now at the position of maximum nuclear recoil.

Unfortunately we have no guarantee that this analysis of the 2C results is applicable to the results of the complex calculations of the DS3C and CCC methods. However, the fact that these two methods are completely different in their conception, that they agree qualitatively with each other and with the modified 2C results of figure 11 in predicting the shape of the angular distribution, we suggest is compelling evidence that it is so. In that case, the two-peak

structure at this energy has little to do with recoil, or perhaps even binary, scattering processes. Rather it arises from an interplay of spatial symmetries, electron repulsion and spin averaging.

4. Conclusions

We have performed a systematic study of electron-impact ionization of atomic hydrogen at an incident energy of 27.2 eV. Three different kinematic regions of the outgoing electrons have been considered, ranging from highly asymmetric to equal energy-sharing. Generally, agreement between the spin-unresolved experiment and the DS3C and CCC theories is good. However, the differences between the CCC and DS3C theories are particularly magnified by consideration of spin-resolved cross sections. Given the substantial progress made by theory in the recent years it is clear that experiment needs to be that much more detailed in order to be able to distinguish between competing theoretical approaches. Clearly, spin-resolved (e, 2e) measurements, as done by Baum *et al* (1992), are most desirable from a theoretical point of view. We are particularly looking forward to the work in this area of the Bielefeld group.

Acknowledgments

Support by the DFG under contract SFB 276 (Freiburg) is gratefully acknowledged. The CCC calculations were performed at the South Australian Centre for High Performance Computing and Communications. Support of the Australian Research Council and the US National Science Foundation is gratefully acknowledged.

Note added in proof. In a recent work, Jones and Madison (1998) have shown that including initial-state distortion effects in a 3C-type calculation results in improved agreement with the *shape* of the measured cross sections, compared with the 3C results shown in this work. Unfortunately, the absolute values of the cross sections predicted by Jones and Madison differ substantially from those anticipated by the DS3C and the CCC methods. Therefore, an experimental verification of the absolute values of the cross sections would be most useful. From a mathematical analysis of the theory presented by Jones and Madison it is clear, however, that this theory yields cross sections that vanish exponentially with vanishing excess energies, a fact which is at variance with experimental findings. This behaviour is due to the properties of the 3C wavefunction (Berakdar 1996b) at low energies.

References

Bartschat K and Bray I 1996 *J. Phys. B: At. Mol. Opt. Phys.* **29** L577
Baum G, Blask W, Freienstein P, Frost L, Hesse S, Raith W, Rappolt P and Streun M 1992 *Phys. Rev. Lett.* **69** 3037
Berakdar J 1996a *Phys. Rev.* A **53** 2314
——1996b *Aust. J. Phys.* **49** 1095
——1997 *Phys. Rev.* A **55** 800
——1997 *Phys. Rev.* A **56** 370
Berakdar J, Röder J, Briggs J S and Ehrhardt H 1996 *J. Phys. B: At. Mol. Opt. Phys.* **29** 6203
Botero J and Macek J H 1994 *Phys. Rev. Lett.* **68** 576
Brauner, M, Briggs, J S and Klar H 1989 *J. Phys. B: At. Mol. Opt. Phys.* **22** 2265
Brauner M, Briggs J S, Klar H, Broad J T, Rösel T, Jung K and Ehrhardt H 1991 *J. Phys. B: At. Mol. Opt. Phys.* **24** 657
Bray I 1997 *Phys. Rev. Lett.* **78** 4721
Bray I and Fursa D V 1996 *Phys. Rev.* A **54** 2991
Bray I and Stelbovics A T 1992 *Phys. Rev.* A **46** 6995
——1993 *Phys. Rev. Lett.* **70** 746
Briggs J S 1989 *Comment. At. Mol. Phys.* **23** 155
Ehrhardt H, Knoth G, Schlemmer P and Jung K 1985 *Phys. Lett.* A **110** 92
Garibotti G and Miraglia J E 1980 *Phys. Rev.* A **21** 572
Joachain C J 1986 *Comment. At. Mol. Phys.* **17** 261

Jones S and Madison D H 1998 *Phys. Rev. Lett.* **81** 2886
Madison D H, Calhoun R V and Shelton W N 1977 *Phys. Rev.* A **16** 552
McCarthy I E and Weigold E 1995 *Electron–Atom Collisions* (Cambridge: Cambridge University Press)
Röder J 1996 Private communication
Röder J, Rasch J, Jung K, Whelan C T, Ehrhardt H, Allan R J and Walters H R J 1996 *Phys. Rev.* A **53** 225
Rost J M 1998 *Phys. Rep.* **297** 274
Shah M B, Elliott D S and Gilbody H B 1987 *J. Phys. B: At. Mol. Phys.* **20** 3501
Simon B 1978 *Int. J. Quantum Chem.* **14** 529
Wannier G 1953 *Phys. Rev.* **90** 817
Whelan C T, Allan R J, Walters H R J and Zhang X *(e,2e) and Related Processes* ed C T Whelan *et al* (Dordrecht: Kluwer) p 1